Anisotropic attenuation analysis of crosshole data generated during hydraulic fracturing

BHARATH SHEKAR and ILYA TSVANKIN, Colorado School of Mines

Attenuation of seismic waves is sensitive to the physical properties of the subsurface and has been observed in vertical seismic profiling (VSP) and reflection data. De et al. (1994) report measurements of the P- and S-wave quality factors from VSP surveys and sonic logs. Klimentos (1995) measures compressional and shear attenuation from sonic logs in sandstone formations with variable oil, water, and gas saturation and observes that Q_P and Q_S can be used for pore-fluid discrimination. Maultzsch et al. (2007) evaluate P-wave azimuthal attenuation anisotropy from 3D VSP data acquired over a fractured hydrocarbon reservoir and infer fracture directions from attenuation analysis. Attenuation anisotropy has also been observed in P-wave reflection data (Clark et al., 2009; Vasconcelos and Jenner, 2005).

Seismic attenuation is most commonly measured using the spectral-ratio method. Zhu et al. (2007) extend the spectral-ratio method to anisotropic media and apply it to physical modeling data acquired for a transversely isotropic (TI) sample. Computing spectral ratios helps eliminate the source spectrum and can be used to obtain accurate effective and interval attenuation coefficients of P- and S-waves in layered anisotropic media (Behura and Tsvankin, 2009a; Shekar and Tsvankin, 2011).

Here, we present a case study with crosshole data generated by perforation shots in a horizontal borehole and recorded in a vertical borehole. The spectral-ratio method applied to all pairs of traces yields a system of equations for the P-wave angle-dependent attenuation coefficient. Since the acquisition aperture is narrow, we approximate the directional dependence of the attenuation coefficient by a quadratic polynomial of the polar and azimuthal angles. The inversion results show that taking attenuation anisotropy into account reduces the data misfit and reveals variations of the attenuation coefficient between perforation stages. Analysis of the shear-wave attenuation coefficient is hampered by the generally poor quality of S-wave data. Although interpretation of the attenuation measurements is not straightforward, it provides indications of temporal changes related to hydraulic fracturing.

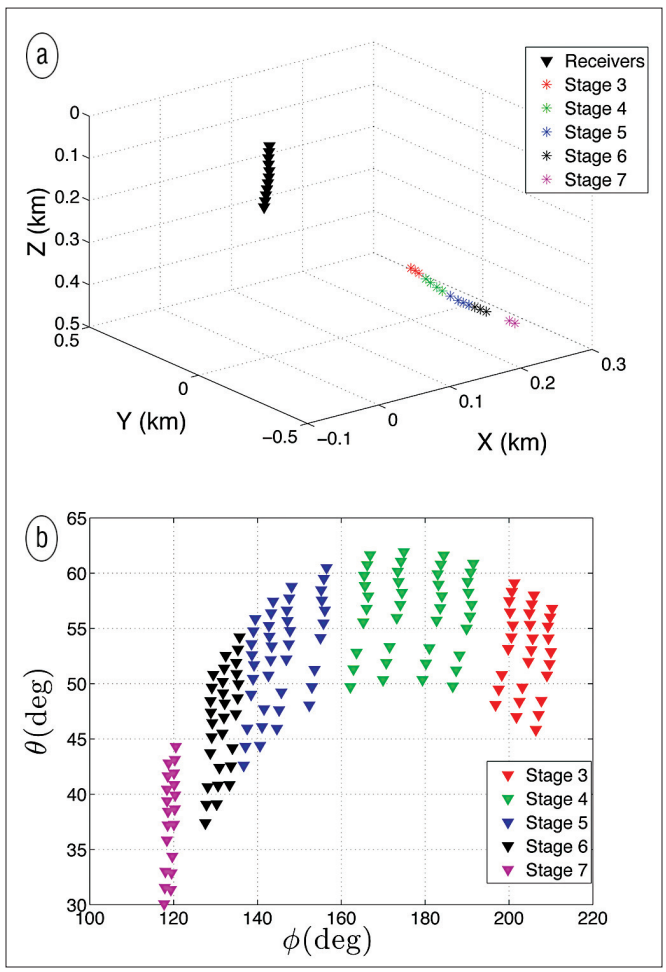

Figure 1. *Acquisition geometry of the experiment; the x-axis points east. The shots in a horizontal borehole are denoted by stars, with different colors corresponding to different stages. The receivers in a vertical borehole are marked by black triangles. The shot and receiver positions are plotted (a) in Cartesian coordinates and (b) as functions of the polar (θ) and azimuthal (ϕ) angles of the source-receiver line.*

Methodology

The data used in our study were generated in a tight shale-gas reservoir by perforation shots fired at regular intervals in a horizontal borehole. The wavefield was recorded by 10 multicomponent receivers placed at different depths in a vertical (monitor) borehole (Figure 1). The perforation shots were grouped into successive "stages", as borehole perforations at each stage were followed by hydraulic stimulation of the perforation-induced fractures.

Multicomponent shot gathers were rotated to maximize the energy of the direct P-waves (Figure 2). After picking the P-wave arrivals, we applied a tapered cosine window around the signal. The amplitude spectra of P-waves excited by one of the perforation shots and recorded by two geophones are shown in Figure 3. The spectrum of the event with the longer raypath is shifted towards lower frequencies, which indicates the influence of attenuation.

In our analysis we have to operate with effective attenuation coefficients along each raypath (i.e., ignore heterogeneity between the source and receiver). The ray-theoretical frequency-domain amplitude of the P-wave propagating between the ith source and the jth receiver in a homogeneous, anisotropic, attenuative medium can be written as

Editor's Note: This article was expanded by the authors from "Anisotropic attenuation analysis of a cross-hole data set" by Bharath Shekar and Ilya Tsvankin, SEG Expanded Abstracts 30, 474 (2011), doi:10.1190/1.3628125.

$$|U_{ij}| = S_i(\omega)\, \mathcal{G}_{ij}\, e^{-k^I_{ij}\, x_{ij}}, \tag{1}$$

where $S_i(\omega)$ represents the source spectrum and G_{ij} (assumed to be frequency-independent) incorporates the geometric spreading and transmission coefficients along the raypath and the source/receiver directivity functions. The coefficient k^I_{ij} is the imaginary part of the P-wave *group* wavenumber along the raypath for the source-receiver pair *ij*, and x_{ij} is the raypath length. According to the results of Behura and Tsvankin (2009b), Equation 1 can be rewritten in terms of the normalized phase attenuation coefficient A_{ij} in the following way:

$$|U_{ij}| = S_i(\omega)\, \mathcal{G}_{ij}\, e^{-\omega\, A_{ij}\, t_{ij}}, \tag{2}$$

where ω is the angular frequency and t_{ij} is the traveltime. The coefficient A_{ij} corresponds to the phase direction of the ray connecting the source and receiver.

Since the perforation shots were not timed, the arrival times picked on the shot gathers (e.g., in Figure 2) do not correspond to the actual traveltimes t_{ij} between the sources and receivers. Grechka and Duchkov (2011) estimate the origin times of the perforation shots by building homogeneous anisotropic velocity models. However, their results indicate that the origin times can be obtained with reasonable accuracy by assuming the medium to be homogeneous and isotropic. Hence, we estimate the origin time t_0 and the velocity V of the direct P-waves by using the following system of equations for each shot (index *i*):

$$t^p_{ij} = t_0 + \frac{d_{ij}}{V}, \tag{3}$$

where t^p_{ij} is the traveltime for the j^{th} receiver picked on the shot gather and d_{ij} is the known source-receiver distance. Hence, the actual traveltime will be given by $t_{ij} = t^p_{ij} - t_0$.

The logarithmic spectral ratio for two P-wave arrivals excited by the *i*th source and recorded by receivers *j* and *k* has the form (Equation 2):

$$\ln \bar{U} = \ln \left| \frac{U_{ij}}{U_{ik}} \right| = \ln \mathcal{G} - \omega\, s_{ijk}, \tag{4}$$

$$s_{ijk} = A_{ij}\, t_{ij} - A_{ik}\, t_{ik}, \tag{5}$$

where $G = G_{ij}/G_{ik}$ is assumed to be frequency-independent. Note that the source spectrum in Equation 4 is eliminated. Hence, the slope of the logarithmic spectral ratio for two source-receiver pairs yields the quantity s_{ijk}, which depends on the corresponding phase attenuation coefficients.

The spectral ratio computed for the two amplitude spectra from Figure 3a is displayed in Figure 3b. The bandwidth used in the spectral-ratio method has to be chosen in a frequency range where the signal-to-noise ratio is sufficiently high (e.g., 30–350 Hz in Figure 3a). The estimate of s_{ijk} is found from least-squares regression.

In homogeneous isotropic media, the attenuation coefficient *A* is constant for all source-receiver pairs. If the medium is anisotropic, the coefficient *A* varies with the orientation of the source-receiver line. By treating all attenuation coefficients as independent quantities, we can set up a system of linear equations for each stage. For example, the third stage includes three shots and 10 receivers, and the system of linear equations that includes the results for all source-receiver pairs is

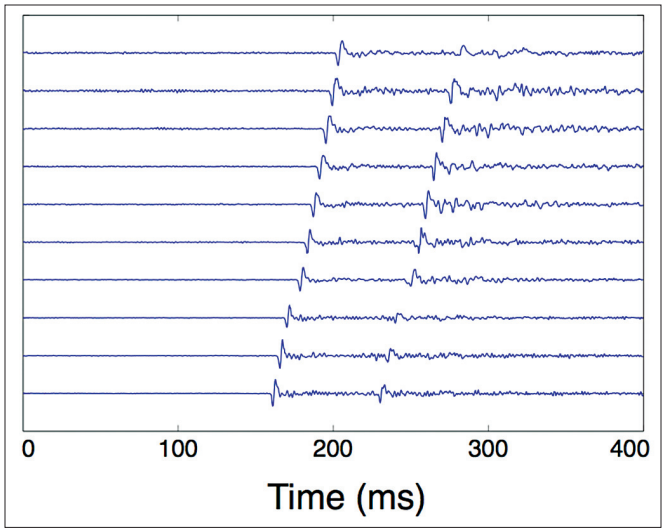

Figure 2. *Shot gather from a perforation shot in stage 3. The first arrivals with a linear moveout are the direct P-waves. The recorded displacement components were rotated to enhance P-wave energy.*

$$s_{ijk} = A_{ij}\, t_{ij} - A_{ik}\, t_{ik};\ 1 \le i \le 3,\ 1 \le j < k \le 10, \tag{6}$$

where, as before, the index *i* denotes the source, while *j* and *k* denote the receivers. Linear system 6 is overdetermined (there are 135 equations for 30 unknowns), but ill-conditioned due to closely spaced receivers and small differences between the arrival times. Hence, the attenuation coefficient along each raypath cannot be resolved individually. As mentioned above, this analysis assumes the medium to be homogeneous. In the presence of heterogeneity, the recovered attenuation coefficients represent effective quantities for each source-receiver pair. To reduce the number of unknowns but still honor attenuation anisotropy, we need to express attenuation coefficients as functions of angle. It has been shown in the literature that most fractured reservoirs can be well approximated by models with orthorhombic symmetry (Tsvankin and Grechka, 2011, and references therein). Zhu and Tsvankin (2006, 2007) obtain approximate phase attenuation coefficients of P- and S-waves in homogeneous TI and orthorhombic media in terms of Thomsen-style attenuation-anisotropy parameters. Their expression for the P-wave phase attenuation coefficient in orthorhombic media with the symmetry planes aligned with the Cartesian coordinate planes is:

$$A_P(\theta, \phi) = A_{P0}[1 + \delta_Q(\phi)\, \sin^2\theta \cos^2\theta + \epsilon_Q(\phi) \sin^4\theta], \tag{7}$$

where A_{P0} is the vertical attenuation coefficient, θ is the polar angle, ϕ is the azimuth with respect to the x_1-axis, and $\delta_Q(\phi)$ and $\varepsilon_Q(\phi)$ depend on the attenuation-anisotropy parameters $\delta_Q^{(1,2,3)}$ and $\varepsilon_Q^{(1,2)}$ defined in Zhu and Tsvankin (2007).

Since Equation 7 is derived in the linearized weak-anisotropy approximation, the phase angle can be replaced with the group

	P_1 $\times 10^{-3}$	P_2 $\times 10^{-3}$	P_3 $\times 10^{-3}$	P_4 $\times 10^{-3}$	P_5 $\times 10^{-3}$	P_6 $\times 10^{-3}$
Stage 3	26.7 ± 2.0	–	–117.6 ± 21.9	–40.8 ± 8.6	–	49.4 ±13.9
Stage 4	24.2 ± 1.2	–	–72.0 ± 14.4	–20.8 ± 4.4	–	24.9 ± 7.1
Stage 5	22.1 ± 1.6	–	–	–21.6 ± 6.7	–	27.5 ± 10.2
Stage 6	7.3 ± 0.9	–	–106.2 ± 14.9	–	–	163.6 ± 25.7
Stage 7	15.8 ± 0.7	–	107.5 ± 15.9	40.7 ± 21.5	–	354.9 ± 60.8

Table 1. *Inverted elements of the model vector and their standard deviations for each stage. The dashes indicate the coefficients rejected by the best-subset regression.*

angle of the source-receiver direction (see Figure 1b). Our analysis shows that, due to the limited angular coverage and absence of near-vertical raypaths, the attenuation-anisotropy parameters cannot be resolved with sufficient accuracy. Therefore, instead of using Equation 7, we represent A_{ij} by a second-order polynomial of the polar (θ_{ij}) and azimuthal (ϕ_{ij}) angles of the corresponding source-receiver direction (Figure 1b):

$$A_{ij} = P_1 + P_2\,\tilde{\theta}_{ij} + P_3\,\tilde{\theta}_{ij}^2 + P_4\,\tilde{\phi}_{ij} + P_5\,\tilde{\phi}_{ij}^2 + P_6\,\tilde{\theta}_{ij}\,\tilde{\phi}_{ij}, \quad (8)$$

$$\tilde{\theta}_{ij} = \theta_{ij} - \theta_c, \;\; \tilde{\phi}_{ij} = \phi_{ij} - \phi_c, \quad (9)$$

where the mean values of the polar (θ_c) and azimuthal (ϕ_c) angles for a given stage correspond to the "central ray" for that stage. Substituting Equation 8 into Equation 6, we obtain the following system of linear equations:

$$\begin{aligned} s_{ijk} &= P_1\,(t_{ij} - t_{ik}) + P_2\,(t_{ij}\,\tilde{\theta}_{ij} - t_{ik}\,\tilde{\theta}_{ik}) \\ &+ P_3\,(t_{ij}\,\tilde{\theta}_{ij}^2 - t_{ik}\,\tilde{\theta}_{ik}^2) + P_4\,(t_{ij}\,\tilde{\phi}_{ij} - t_{ik}\,\tilde{\phi}_{ik}) \\ &+ P_5\,(t_{ij}\,\tilde{\phi}_{ij}^2 - t_{ik}\,\tilde{\phi}_{ik}^2) + P_6\,(t_{ij}\,\tilde{\theta}_{ij}\,\tilde{\phi}_{ij} - t_{ik}\,\tilde{\theta}_{ik}\,\tilde{\phi}_{ik}). \end{aligned} \quad (10)$$

In Equation 10, the only unknowns are the coefficients P_1, P_2, P_3, P_4, P_5, and P_6, which are computed from least-squares regression. Assuming isotropic (angle-independent) attenuation yields a higher rms error, so taking anisotropy into account is essential to fit the data.

Inversion results

The best-fit inverted coefficients and their standard deviations are listed in Table 1. Directional dependence of attenuation is non-negligible, with the polar anisotropy more pronounced than azimuthal anisotropy. The only exception is stage 5, which exhibits relatively weak attenuation anisotropy. The attenuation coefficient for stage 6 is substantially lower than that for the other stages, most likely due to the influence of heterogeneity and/or measurement errors.

The analytic attenuation coefficient for orthorhombic media (Equation 7) can be expanded in a Taylor series around the mean values of the polar (θ) and azimuthal (ϕ) angles for each stage. In principle, if the orientation of the symmetry planes is known, the six polynomial coefficients in Equation 8 can be used to uniquely determine all six Thomsen-style attenuation parameters contributing to Equation 7. However, due to the trade-offs between the coefficients of the polynomial, the attenuation-anisotropy parameters cannot be resolved individually. Physically, the range of the polar and azimuthal angles in the experiment is too narrow to reconstruct the attenuation coefficient for all propagation directions.

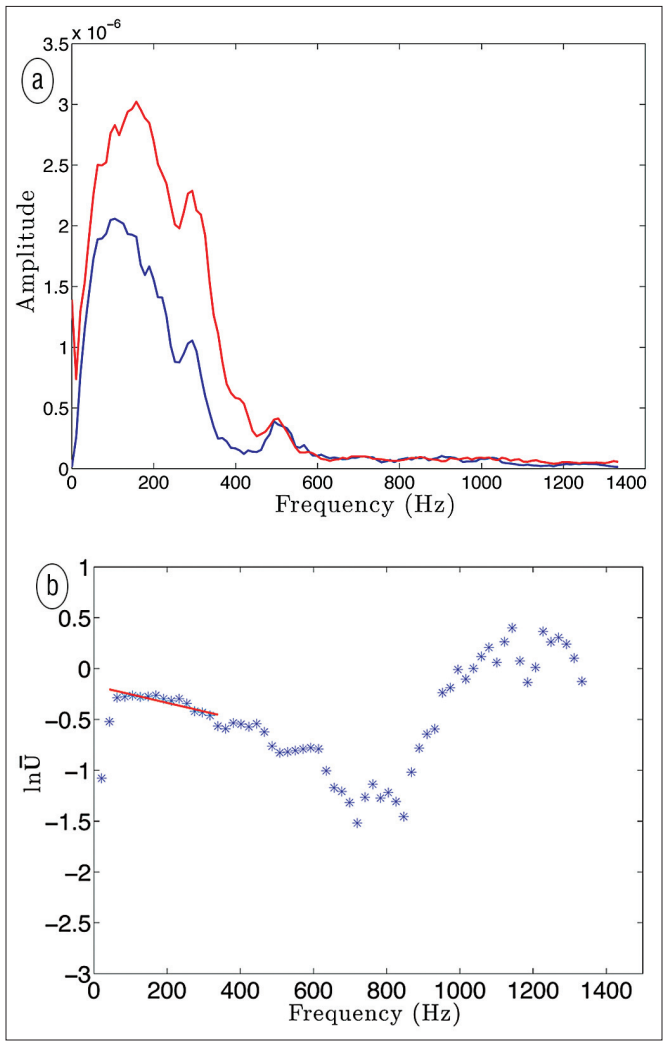

Figure 3. *(a) Amplitude spectra of two P-wave arrivals excited by one of the shots in stage 3 and recorded by the shallowest (red curve) and deepest (blue curve) geophones. (b) The logarithmic spectral ratio of the amplitude spectra from (a) (blue stars) and the best-fit straight line (red) in the selected frequency band.*

It is essential to evaluate the sensitivity of the inversion results to uncertainties in the origin times. We added 100 realizations of Gaussian noise with a standard deviation of 20 time samples to

	P_1 $\times 10^{-3}$	P_2 $\times 10^{-3}$	P_3 $\times 10^{-3}$	P_4 $\times 10^{-3}$	P_5 $\times 10^{-3}$	P_6 $\times 10^{-3}$
Stage 3	26.5 ± 0.6	–	–116.4 ± 6.0	–40.0 ± 3.0	–	49.6 ± 6.7
Stage 4	24.1 ± 0.3	–	–70.2 ± 2.7	–20.3 ± 1.2	–	24.3 ± 2.6
Stage 5	22.0 ± 0.2	–	–	–21.5 ± 1.3	–	28.0 ± 2.6
Stage 6	7.3 ± 0.1	–	–106.2 ± 3.6	–	–	163.7 ± 6.1
Stage 7	15.8 ± 0.1	–	107.7 ± 2.7	40.7 ± 0.9	–	–355.3 ± 9.8

Table 2. *Sensitivity of the inversion results to errors in the origin times. The standard deviations are computed by contaminating the origin times with 100 realizations of Gaussian noise that has a standard deviation of 20 time samples. The standard deviations do not include errors of the spectral-ratio method taken into account in Table 1.*

the origin times and estimated the coefficients in Equation 10 for each of these realizations. The mean values and standard deviations of the elements of the vector **m** are listed in Table 2. Clearly, the inversion results are weakly influenced by errors in the origin times. In computing the standard deviations, we did not include the errors of the spectral-ratio method. In fact, comparison of Tables 1 and 2 shows that the inverted attenuation coefficient is more sensitive to noise in the spectral-ratio estimates.

The mean values and standard deviations of the attenuation coefficients A_p for all source-receiver pairs are shown in spherical coordinates in Figure 4. Clearly, effective attenuation between the boreholes decreases with the stage number. This variation in attenuation is likely related to the changes in the medium due to hydraulic fracturing and pumping of fluids through the rock volume. Fluid diffusion can be monitored using microseismic data, which were not available to us.

Analysis of shear-wave data

It would be beneficial to combine P-wave attenuation measurements with those for S-waves. The plane P-wave polarization vector in anisotropic media is normal to the plane defined by the polarization vectors of the two split shear waves. As described above, we rotate the three displacement components to maximize the direct P-wave energy on one of them (e.g., Figure 2). The other two components are expected to contain S-waves and can be rotated further to identify the fast and slow shear modes. However, due to the generally poor shear-wave data quality (e.g., Figure 5b), this rotation enhances only one of the split S-waves

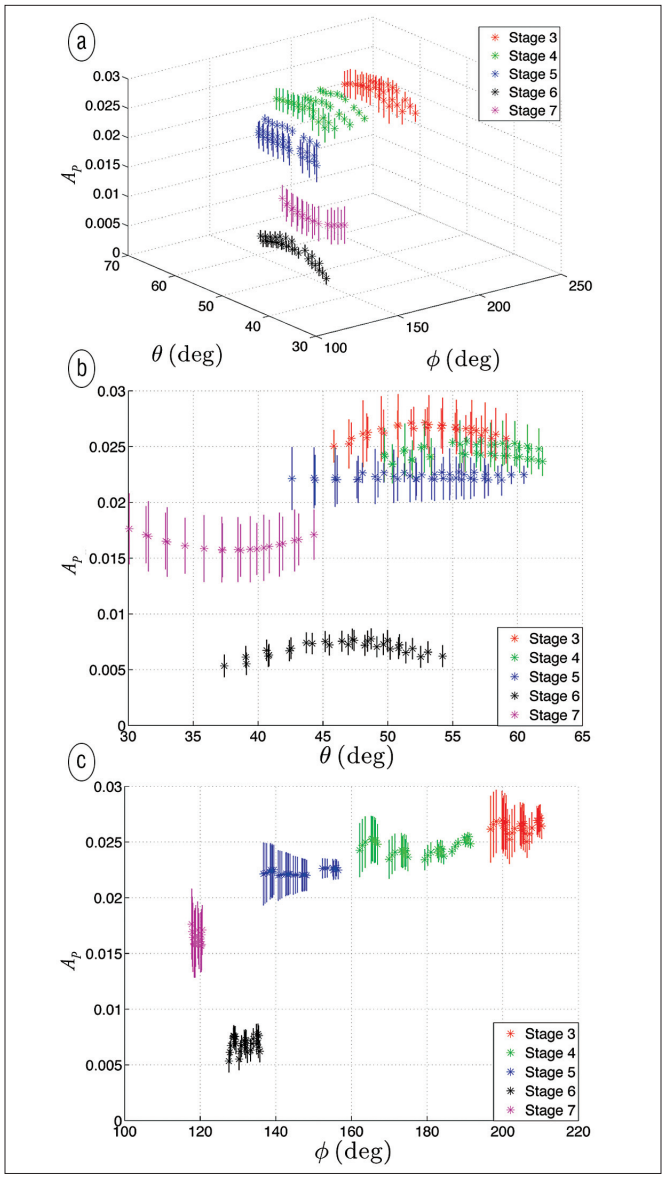

Figure 4. *(a) P-wave attenuation coefficients (stars of different colors) for all source-receiver pairs in spherical coordinates. (b) Variation of* A_p *with the polar angle obtained as the projection of plot (a) onto the* $[A_p, \theta]$*-plane. (c) Variation of* A_p *with the azimuthal angle.*

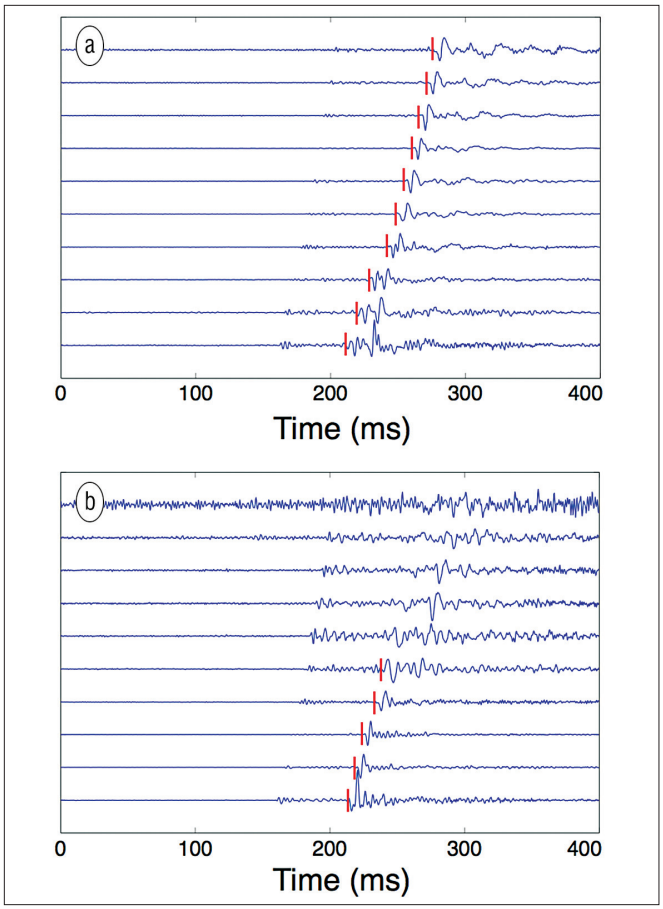

Figure 5. *Record of a perforation shot in (a) stage 3 and (b) stage 4 after rotation designed to enhance direct S-waves. The first arrivals are indicated by red ticks. The shot gather on plot (a) was obtained from the same data as the gather in Figure 2.*

(Figure 5). The shot gather in Figure 5a was generated by rotating the same raw data as the gather in Figure 2; the second arrivals in Figure 2 correspond to the first arrivals in Figure 5a. If the first arrivals in Figure 5a represent direct S-waves, they should not be so prominent in Figure 2, which displays the displacement components rotated to enhance direct P-wave energy. Hence, it is unclear whether the first arrivals in Figure 5a represent direct S-waves.

Conclusions

We introduced a methodology for estimating the directionally dependent P-wave attenuation coefficient from crosshole data acquired for a relatively narrow range of propagation angles. A string of receivers in a vertical borehole was used to record the wavefield excited by perforation shots set off in a horizontal hole to induce hydraulic fracturing. The attenuation coefficient was represented as a quadratic polynomial of the polar and azimuthal angles, and the polynomial coefficients were estimated by applying the spectral-ratio method to pairs of traces. The data for each stage of perforation shots were processed separately, with the attenuation coefficient expanded around the corresponding "central ray." The inversion results show that taking anisotropy into account substantially improves fitting of the attenuation measurements. The angular variation of the attenuation coefficient is more pronounced in the vertical plane, so polar attenuation anisotropy is stronger than azimuthal anisotropy. Clearly, more robust estimation of attenuation anisotropy requires data with better angular coverage. Meaningful attenuation analysis of shear waves is hindered by the difficulty in separating the split S-waves and by the generally poor quality of shear data.

The mean value of the attenuation coefficient decreases with successive stages of hydraulic fracturing and stimulation. This could be due to the diffusion of stimulant fluids in the induced fractures, which stiffens the medium and makes it less attenuative. Microseismic monitoring can delineate the extent of the zones of fluid diffusion, which should help verify this hypothesis. Because the reservoir formation is made up mostly of shale, it is likely to exhibit intrinsic attenuation anisotropy, which may complicate analysis of the attenuation signature of hydraulic fracturing. If multicomponent, multiazimuth, walkaway VSP data are available, the local anisotropy parameters can be estimated at the receiver ar-

ray (Tsvankin and Grechka, 2011, and references therein), which can help in calibrating our model. TLE

References

Behura, J. and I. Tsvankin, 2009a, Estimation of interval anisotropic attenuation from reflection data: Geophysics, **74**, no. 6, A69–A74, http://dx.doi.org/10.1190/1.3191733.

Behura, J. and I. Tsvankin, 2009b, Role of the inhomogeneity angle in anisotropic attenuation analysis: Geophysics, **74**, no. 5, WB177–WB191, http://dx.doi.org/10.1190/1.3148439.

Clark, R. A., P. M. Benson, A. J. Carter, and C. A. G. Moreno, 2009, Anisotropic P-wave attenuation measured from a multi-azimuth surface seismic reflection survey: Geophysical Prospecting, **57**, no. 5, 835–845, http://dx.doi.org/10.1111/j.1365-2478.2008.00772.x.

De, G. S., D. F. Winterstein, and M. A. Meadows, 1994, Comparison of P- and S-wave velocities and Q's from VSP and sonic log data: Geophysics, **59**, no. 10, 1512–1529, http://dx.doi.org/10.1190/1.1443541.

Grechka, V. and A. Duchkov, 2011, Narrow-angle representations of the phase and group velocities and their applications in anisotropic velocity-model building for microseismic monitoring: Geophysics, **76**, no. 6, WC127–WC142, http://dx.doi.org/10.1190/geo2010-0408.1.

Klimentos, T., 1995, Attenuation of P- and S-waves as a method of distinguishing gas and condensate from oil and water: Geophysics, **60**, no. 2, 447–458, http://dx.doi.org/10.1190/1.1443782.

Maultzsch, S., M. Chapman, E. Liu, and X.-Y. Li, 2007, Modelling and analysis of attenuation anisotropy in multi-azimuth VSP data from Clair field: Geophysical Prospecting, **55**, no. 5, 627–642, http://dx.doi.org/10.1111/j.1365-2478.2007.00645.x.

Shekar, B. and I. Tsvankin, 2011, Estimation of shear-wave interval attenuation from mode-converted data: Geophysics, **76**, no. 6, D11–D19, http://dx.doi.org/10.1190/geo2010-0415.1.

Tsvankin, I. and V. Grechka, 2011, Seismology of azimuthally anisotropic media and seismic fracture characterization: SEG.

Vasconcelos, I. and E. Jenner, 2005, Estimation of azimuthally varying attenuation from wide-azimuth P-wave data: 75th Annual International Meeting, SEG, Expanded Abstracts, 123–126.

Zhu, Y. and I. Tsvankin, 2006, Plane-wave propagation in attenuative transversely isotropic media: Geophysics, **71**, no. 2, T17–T30, http://dx.doi.org/10.1190/1.2187792.

Zhu, Y. and I. Tsvankin, 2007, Plane-wave attenuation anisotropy in orthorhombic media: Geophysics, **72**, no. 1, D9–D19, http://dx.doi.org/10.1190/1.2387137.

Zhu, Y., I. Tsvankin, P. Dewangan, and K. V. Wijk, 2007, Physical modeling and analysis of P-wave attenuation anisotropy in transversely isotropic media: Geophysics, **72**, no. 1, D1–D7, http://dx.doi.org/10.1190/1.2374797.

Acknowledgments: We thank Shell E&P Company and EnCana for providing the data. We are grateful to Vladimir Grechka (Shell), Serge Shapiro (Free University of Berlin), and the members of the A(nisotropy)-Team of the Center for Wave Phenomena (CWP), Colorado School of Mines, for fruitful discussions. Support for this work was provided by the Consortium Project on Seismic Inverse Methods for Complex Structures at CWP and by the Research Partnership to Secure Energy for America (RPSEA).

Corresponding author: ilya@dix.mines.edu